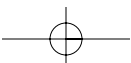
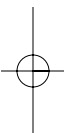


# **PART I**

---

## **ESR FUNDAMENTALS**



---

# 1

---

## CONTINUOUS-WAVE AND PULSED ESR METHODS

GUNNAR JESCHKE

*Max Planck Institute for Polymer Research, Mainz, Germany*

SHULAMITH SCHLICK

*University of Detroit Mercy, Detroit, Michigan*

### Contents

1. Introduction	3
2. Fundamentals of Electron Spin Resonance Spectroscopy	4
2.1. Basic Principles	4
2.2. Anisotropic Hyperfine Interaction and $g$ -Tensor	10
2.3. Isotropic Hyperfine Analysis	12
2.4. Environmental Effects on $g$ - and Hyperfine Interaction	12
2.5. Accessibility to Paramagnetic Quenchers	13
2.6. Line Shape Analysis for Tumbling Nitroxide Radicals	15
3. Multifrequency and High-Field ESR	16
4. Pulsed ESR Methods	18
Acknowledgments	22
References	22

### 1. INTRODUCTION

Electron spin resonance (ESR) is a spectroscopic technique that detects the transitions induced by electromagnetic radiation between the energy levels of electron

---

*Advanced ESR Methods in Polymer Research*, edited by Shulamith Schlick.  
Copyright © 2006 John Wiley & Sons, Inc.

spins in the presence of a static magnetic field. The method can be applied to the study of species containing one or more unpaired electron spins; examples include organic and inorganic radicals, triplet states, and complexes of paramagnetic ions. Spectral features, such as resonance frequencies, splittings, line shapes, and line widths, are sensitive to the electronic distribution, molecular orientations, nature of the environment, and molecular motions. Theoretical and experimental aspects of ESR have been covered in a number of books,<sup>1-8</sup> and reviewed regularly.<sup>9-11</sup>

Currently available textbooks and monographs are written for students and scientists that specialize in the development of ESR technique and its application to a broad range of samples. Nowadays, however, research groups are interested in a specific field of applications, such as polymer science, and apply more than one characterization method to the materials of interest. An introduction to ESR that targets such an audience needs to be shorter, less mathematical, and focused on application rather than methodological issues. This chapter is an attempt to provide such a short introduction on the application of ESR spectroscopy to problems in polymer science.

Organic radicals occur in polymers as intermediates in chain-growth and depolymerization reactions,<sup>12-15</sup> or as a result of high-energy irradiation ( $\gamma$ , electron beams).<sup>13,14</sup> Paramagnetic transition metal ions are present in a number of functional polymer materials, such as catalysts and photovoltaic devices.<sup>16</sup> However, much of the modern ESR work in polymer science focuses on diamagnetic materials that are either doped with stable radicals as “spin probes”, or labeled by covalent attachment of such radicals as “spin labels” to polymer chains.<sup>9,17-22</sup> This chapter therefore treats the *basic* concepts that are required to understand ESR spectra of a broad range of organic radicals and transition metal ions, and describes more advanced concepts as applied to the most popular class of spin probes and labels: nitroxide radicals.

## 2. FUNDAMENTALS OF ELECTRON SPIN RESONANCE SPECTROSCOPY

### 2.1. Basic Principles

Spins are magnetic moments that are associated with angular momentum; they interact with external magnetic fields (Zeeman interaction) and with each other (couplings). In most cases, the Zeeman interaction of the electron spin is the largest interaction in the spin system (high-field limit). The electron Zeeman (EZ) interaction can generally be described by the Hamiltonian below,

$$\mathcal{H}_{EZ} = \beta_e \mathbf{B}_0 \mathbf{g} \mathbf{S} \quad (1)$$

where  $\mathbf{S}$  is the spin vector operator,  $\mathbf{B}_0$  is the transposed magnetic field vector in gauss (G) or tesla (1 T =  $10^4$  G),  $\beta_e$  is the Bohr magneton equal to  $9.274 \times 10^{-21}$  ergG<sup>-1</sup> (or  $9.274 \times 10^{-24}$  JT<sup>-1</sup>), and  $\mathbf{g}$  is the  $g$  tensor. For a free electron,  $g$  is simply the number  $g_e = 2.002319$ . The transition energy is then  $\Delta E = h\nu_{mw} = g_e \beta_e B_0$ , where  $B_0$  is the magnitude of the magnetic field. Typical values are  $B_0 \approx 0.34$  T (3400 G) corresponding to microwave (mw) frequencies of  $\approx 9.6$  GHz (X band), or  $B_0 \approx 3.35$  T corresponding to mw frequencies of  $\approx 94$  GHz (W band).

The  $g$ -value of a bound electron generally exhibits some deviation from  $g_e$  that is mainly due to interaction of the spin with orbital angular momentum of the unpaired electron (spin-orbit coupling). Spin-orbit coupling is a relativistic effect that tends to increase with increasing atomic number of the nuclei that contribute atomic orbitals to the singly occupied molecular orbital. Therefore,  $g$ -values deviate more strongly from  $g_e$  for transition metal complexes than for organic radicals. As the orbital angular momentum is quenched in the ground state of molecules, spin-orbit coupling comes about only by admixture of excited orbitals. Such admixture is stronger for low-lying excited states, which are relevant, for example, if the unpaired electron has high density at an oxygen atom. Oxygen-centered organic radicals thus tend to have higher  $g$ -values than carbon-centered ones.

As the orbital angular momentum relates to a molecular coordinate frame and the spin is quantized along the magnetic field ( $z$  axis of the laboratory frame), the  $g$ -value depends on the orientation of the molecule with respect to the field. This anisotropy can be described by a second rank tensor with three principal values,  $g_x$ ,  $g_y$ , and  $g_z$ . The corresponding principal axes define the molecular frame. In fluid solutions, molecules tumble with a rotational diffusion rate that is much higher than the differences of the electron Zeeman frequencies between different orientations. In this situation, the  $g$ -value is orientationally averaged and only its isotropic value  $g_{\text{iso}} = (g_x + g_y + g_z)/3$  can be measured. A good overview of isotropic  $g$ -values of organic radicals can be found in Ref. 23; Ref. 5 collects information on  $g$  tensors for transition metal complexes.

The real power of ESR spectroscopy for structural studies is based on the interaction of the unpaired electron spin with nuclear spins. This hyperfine interaction splits each energy level into sublevels and often allows the determination of the atomic or molecular structure of species containing unpaired electrons, and of the ligation scheme around paramagnetic transition metal ions. For a system with  $m$  nuclear spins (identified by index  $k$ ) and a single electron spin, which may be larger than one-half as explained below, the hyperfine Hamiltonian is given in Eq. 2,

$$\mathcal{H}_{\text{hfi}} = h \sum S \cdot A_k \cdot I_k \quad (2)$$

where the  $I_k$  are nuclear spin vector operators and the  $A_k$  are hyperfine tensors in frequency units (Hz). Each hyperfine tensor is characterized by three principal values  $A_x$ ,  $A_y$ , and  $A_z$  and by the relative orientation of its principal axes system with respect to the molecular frame defined by the  $g$ -tensor. This relative orientation is most easily defined by three Euler angles  $\alpha$ ,  $\beta$ ,  $\gamma$ , which correspond to a sequence of rotations about the  $z$  axis (by angle  $\alpha$ ), the new  $y'$  axis (by angle  $\beta$ ), and the final  $z''$  axis (by angle  $\gamma$ ); these rotations transform the principal axes frame of the hyperfine tensor into that of the  $g$ -tensor. The relative orientation is often given as direction cosines, which are the coordinates of unit vectors along the directions of the hyperfine principal axes given in the coordinate frame of the  $g$ -tensor.

Only the isotropic value  $A_{\text{iso}} = (A_x + A_y + A_z)/3$  can be measured in fluid solutions, and is due to the Fermi contact interactions of electrons that reside in an  $s$  orbital of the nucleus under consideration. The contribution of a single orbital is

proportional to the spin population (spin density) in that orbital, to the probability density  $|\psi_0|^2$  of the orbital wave function at its center (inside the nucleus), and to the nuclear  $g$ -value,  $g_n$ . To a very good approximation, the hyperfine couplings for different isotopes of the same element thus have the same ratio as the  $g_n$  values.

Purely anisotropic contributions ( $A_x + A_y + A_z = 0$ ) to the hyperfine coupling result from spin density in  $p$ ,  $d$ , or  $f$  orbitals on the nucleus and from the dipole–dipole interaction  $\mathbf{T}$  between the electron and nuclear spin. If the electron spin is confined to a region that is much smaller than the electron–nuclear distance  $r_{\text{en}}$ , both spins can be treated as point dipoles and the magnitude of  $T$  is proportional to  $r_{\text{en}}^{-3}$ . In this case,  $\mathbf{T}$  has axial symmetry and its principal values are given by  $T_x = T_y = -T$  and  $T_z = 2T$ . Furthermore, if the spin density in  $p$ ,  $d$ , and  $f$  orbitals on that nucleus is negligible, as is the case for protons ( $^1\text{H}$ ), the measurement of the hyperfine anisotropy can provide the electron–nuclear distance  $r_{\text{en}}$ . Any spin density at the nucleus under consideration is negligible if this nucleus is located in a neighboring molecule and does not interact (by van der Waals or hydrogen bonding) with a nucleus on which much spin density is located. Intermolecular distances larger than  $\approx 0.3$  nm can thus be inferred from hyperfine couplings.

For nuclei with significant hyperfine interaction, the other interactions of the nuclear spin also need to be considered. The nuclear Zeeman (NZ) interaction of these spins with the external magnetic field is described in Eq. 3.

$$\mathcal{H}_{\text{NZ}} = -\sum g_{n,k} \beta_n \mathbf{B}_0 \mathbf{I}_k \quad (3)$$

Nuclear spins with  $I > \frac{1}{2}$  have an electric quadrupole moment that interacts with the quadrupole moment of the charge distribution around the nucleus. The Hamiltonian for this nuclear quadrupole (NQ) interaction is given in Eq. 4,

$$\mathcal{H}_{\text{NQ}} = \hbar \sum \mathbf{I}_k \mathbf{Q}_k \mathbf{I}_k \quad (4)$$

where  $\mathbf{Q}_k$  are the traceless ( $Q_x + Q_y + Q_z = 0$ ) nuclear quadrupole tensors. Because the tensor is traceless, this interaction is not detected in fluid media.

Both the nuclear Zeeman and nuclear quadrupole interaction do not depend on the magnetic quantum number  $m_S$  of the electron spin. As the selection rule for ESR transitions is given by Eq. 5,

$$\Delta m_S = \pm 1 \quad \text{and} \quad \Delta m_I = 0 \quad (5)$$

where  $m_I$  is the nuclear spin quantum number, these interactions do not make a first-order contribution to the ESR spectrum. In many cases, they can thus be neglected in spectrum analysis. This situation is illustrated in Fig. 1 for a nitroxide in which the nuclear spin  $I = 1$  of the  $^{14}\text{N}$  atom is coupled to the electron spin  $S = \frac{1}{2}$  that resides mainly in the  $p_z$  orbitals on the N and O atom. The hyperfine coupling causes a splitting of each of the electron spin levels ( $m_S = -\frac{1}{2}$  and  $m_S = +\frac{1}{2}$ ) into three sublevels. When a constant microwave frequency  $\nu_{\text{mw}}$  is irradiated and the magnetic field is swept, three resonance transitions are observed (Fig. 1a). The

nuclear Zeeman interaction shifts both  $m_I = +1$  sublevels to lower and both  $m_I = -1$  sublevels to higher energy, but does not influence the resonance fields where the splitting between the levels with different  $m_S$  and the same  $m_I$  matches the energy of the mw quantum (Fig. 1b).

More generally, the higher sensitivity of ESR experiments can be used for the detection of NMR frequencies by applying both resonant mw and resonant radio frequency (rf) irradiation to the spin system. Such electron nuclear double-resonance (ENDOR) experiments are discussed in Chapter 2.

Transition metal ions can have several unpaired electrons when they are in their high-spin state; examples are Cr(III) ( $3d^3$  configuration,  $S = \frac{3}{2}$ ), Mn(II) ( $3d^5$ ,  $S = \frac{5}{2}$ ),

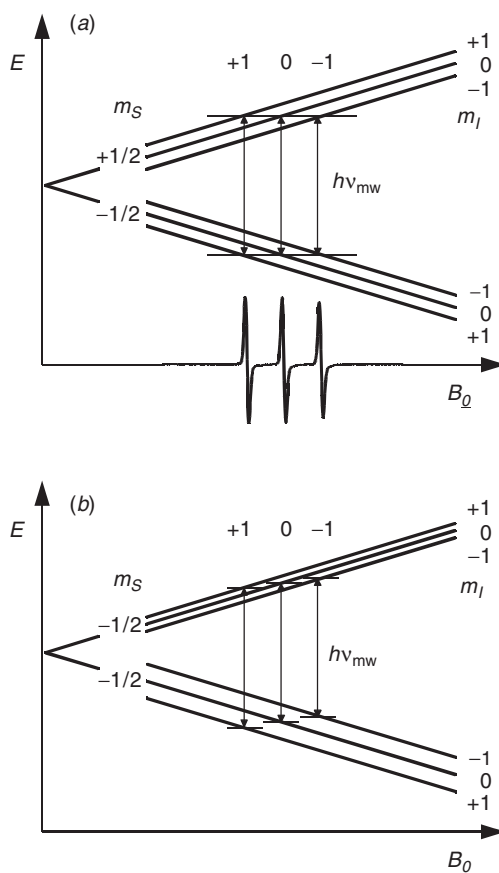


**Fig. 1.** Energy level schemes and ESR spectrum for a spin system of an electron spin  $S = \frac{1}{2}$  coupled to a nuclear spin  $I = 1$  (e.g.,  $^{14}\text{N}$  in a nitroxide). (a) Only the electron Zeeman and hyperfine interactions are considered. (b) The electron Zeeman, hyperfine, and nuclear Zeeman interactions are considered. Note that the splittings match the microwave quantum at the same resonance fields as in part a.

and Fe(III) ( $3d^5$ ,  $S = \frac{5}{2}$ ). The spins of these electrons are tightly coupled and have to be considered as a single group spin  $S > \frac{1}{2}$ . Such an electron group spin also has an electric quadrupole moment. For historical reasons, the electron spin analog of the nuclear quadrupole interaction is termed zero-field splitting (ZFS) and is described by Eq. 6,

$$\mathcal{H}_{\text{ZFS}} = h \mathbf{S} \mathbf{D} \mathbf{S} \quad (6)$$

where  $\mathbf{D}$  is a traceless tensor. Therefore, the ZFS can be characterized by two parameters,  $D = 3D_z/2$  and  $E = (D_x - D_y)/2$ , rather than by giving all three principal values. For axial symmetry  $E = 0$ , and for maximum nonaxiality  $E = D/3$ .

With the exception of transition metal ions at a site with cubic symmetry, the ZFS often exceeds the electron Zeeman interaction at magnetic fields  $< 1$  T, sometimes even at the highest accessible fields (high-spin Fe(III)). In this situation, only the lowest lying doublet of spin states may be populated and only transitions within this doublet can be observed. It is convenient to describe such a doublet by an *effective* spin  $S' = \frac{1}{2}$ . The ZFS of the group spin  $S > \frac{1}{2}$  then contributes to the effective  $g$ -tensor of the spin  $S' = \frac{1}{2}$ . For example, X-band ESR spectra of high-spin Fe(III) in a situation with maximum nonaxiality of the ZFS ( $E = D/3$ ) exhibit a sharp feature at  $g = 4.3$ . Note that unlike the normal  $g$ -tensor, the effective  $g$ -tensor may depend on the applied magnetic field.

For low concentrations of the paramagnetic centers, the electron spins can be considered isolated from each other, and only a single electron spin  $S$  appears in the Hamiltonian. In systems with a high concentration of paramagnetic transition metal ions, this situation can be achieved by diamagnetic dilution with transition ions of the same charge and similar radius and coordination chemistry. However, there are a number of systems that feature coupled electron spins, for example, binuclear metal complexes and biradicals. Any pair of electron spins  $S_k$  and  $S_l$  in such a system interacts through space by dipole–dipole coupling, which is analogous to the dipolar part  $T$  of the hyperfine coupling. The Hamiltonian of the electronic dipole–dipole (DD) coupling is given by Eq. 7,

$$\mathcal{H}_{\text{DD}} = h \sum_k S_k \mathbf{D}_{kl} S_l \quad (7)$$

where the  $\mathbf{D}_{kl}$  are the traceless dipole–dipole tensors. If the two electron spins are far apart, the coupling can be described by a point-dipole approximation in which  $\mathbf{D}_{kl}$  is an axial tensor with principal values  $D_{z,kl} = 2d$  and  $D_{x,kl} = D_{y,kl} = -d$ . As  $d$  is inversely proportional to the cube of the distance  $r_{kl}$  between the two spins, a measurement of this coupling can thus yield the spin–spin distance. Such measurements are discussed in more detail in Chapter 2.

The two electrons can exchange if their wave functions overlap. Even for localized electrons, such an exchange is significant at a distance  $r_{kl} < 1.5$  nm. For an antibonding overlap of the two orbitals, the exchange interaction  $J$  is negative and the triplet state of the pair has lower energy than the singlet state. This is called a ferromagnetic exchange coupling. Consequently, bonding overlap leads to a positive  $J$ , a

lower lying singlet state, and antiferromagnetic coupling. The exchange coupling is not strictly isotropic, but except for electron spins at distances  $< 0.5$  nm, the anisotropic contribution can usually be neglected. For a purely isotropic exchange coupling, the Hamiltonian is written in Eq. 8.

$$\mathcal{H}_{\text{ex}} = h \sum_{kl} J_{kl} \mathbf{S}_k \mathbf{S}_l \tag{8}$$

Unlike the dipole–dipole coupling between the electron spins, the exchange coupling can thus be detected in fluid solutions.

The ESR spectra of monoradicals and mononuclear transition ion complexes can also be influenced by spin exchange, because the wave functions of the electrons overlap for a short time during diffusional collisions of paramagnetic species.<sup>24</sup> At moderate concentrations (1 M or larger), the collisions are so frequent that line broadening and a decrease of the hyperfine splitting can be observed. In macromolecular and supramolecular systems, this effect is sometimes perceptible at lower bulk concentrations, as diffusion may be restricted or local concentrations of some species strongly exceed their bulk concentration. Examples are discussed in Chapter 7.

When the various spin interactions can be separated experimentally or by spectral analysis, ESR spectra become a rich source of information not only on chemical structure of the paramagnetic species, but also on the structure and dynamics of their environment. Figure 2 provides an overview of time scales and length scales that can be accessed in this way.  $T_1$  and  $T_2$  are the longitudinal and transverse relaxation times, respectively.

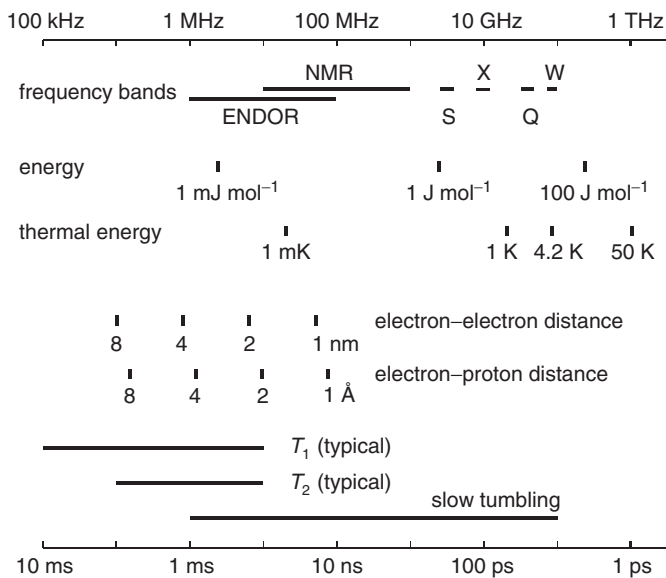


Fig. 2. Frequencies, time scales, energies, and length scales in ESR experiments.

## 2.2. Anisotropic Hyperfine Interaction and $g$ -Tensor

Before considering the analysis of anisotropic solid-state ESR spectra in general, we discuss the orientation dependence of spin interactions of the nitroxide radical as an example. The ESR spectrum of a nitroxide is dominated by the hyperfine interaction of the electron spin with the nuclear spin of the  $^{14}\text{N}$  atom and by  $g$ -shifts due to spin-orbit coupling mainly in the  $2p_z$  orbital of the lone pair on the oxygen atom. The  $^{14}\text{N}$  hyperfine coupling contains a sizeable isotropic contribution due to Fermi contact interaction in the  $2s$  orbital on the nitrogen. An anisotropic contribution comes from the spin density in the nitrogen  $2p_z$  orbital whose lobes are displayed in Fig. 3a. If the external magnetic field  $B_0$  is parallel to these lobes ( $z$  axis of the molecular frame), the hyperfine interaction and thus the splitting within the triplet is large; if it is perpendicular to the lobes, the splitting is small. Conversely,  $g$ -shifts are small when the lobes of the orbital under consideration (here the  $2p_z$  orbital on the oxygen) are parallel to the field and large when they are perpendicular. In the case of a nitroxide, the strongest shift is observed when the field is parallel to the N–O bond, which defines the  $x$  axis of the molecular frame. Hence, the triplets of lines at different orientations of the molecule with respect to the field do not only have different splittings, but their centers are also shifted with respect to each other.

In a macroscopically isotropic sample (all molecular orientations have the same probability), the spectrum consists of contributions from all orientations when the rotational motion is frozen on the time scale of the experiment. As ESR lines are derivative absorption lines, negative and positive contributions from neighboring orientations cancel. Powder spectra are thus dominated by contributions at the minimum and maximum resonance fields, and by contributions at resonance fields that are common to many spins. The latter contribution provides the center line in the nitroxide powder spectrum (Fig. 3b). It corresponds mainly to molecules with nuclear magnetic quantum number  $m_I = 0$  (center line of all triplets, only  $g$ -shift). The detailed shape of this powder spectrum can be simulated, but interpretation is not easy, mainly because hyperfine and  $g$  anisotropy are of similar magnitude.

If one of the two interactions dominates, the spectra can be analyzed more easily. For dominating  $g$  anisotropy (Fig. 4a), signals in the CW ESR spectrum are observed at resonant fields corresponding to the principal values of the  $g$ -tensor:  $g_z$  (low-field edge),  $g_y$ , and  $g_x$  (high-field edge). For a  $g$ -tensor with axial symmetry (wave function of the unpaired electron has at least one symmetry axis  $C_n$  with  $n \geq 3$ ), the intermediate feature coincides with one of the edges (Fig. 4b). For a dominating hyperfine interaction with a nuclear spin  $I = \frac{1}{2}$  the spectrum consists of two of these powder patterns with mirror symmetry about the center of the spectrum (Fig. 4c).

When samples are available as single crystals, spectra corresponding to specific orientations of the paramagnetic center with respect to the external field can be measured separately. The orientation dependence of the spectrum can then be studied systematically and the principal axes frames of the  $A$ - and  $g$ -tensors can be related to the crystal frame. In polymer applications, samples are usually macroscopically isotropic, so that only the principal values of the interactions, and in favorable cases the *relative* orientations of their principal axes frames, can be obtained from spectral simulations. How these frames are related to the molecular geometry then needs to be

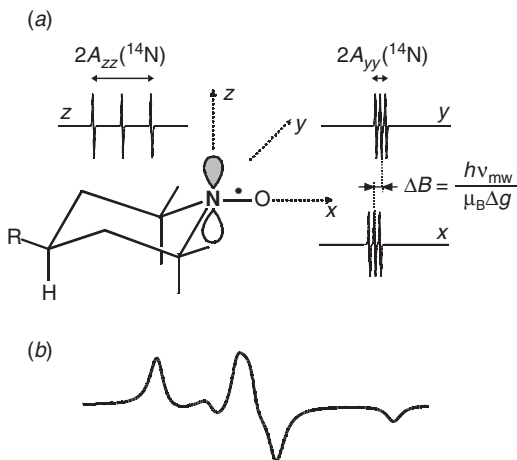


**Fig. 3.** Anisotropic interactions for a nitroxide radical. (a) Molecular frame of the nitroxide molecule and single-crystal ESR spectra along the principal axes of this frame. (b) Powder spectrum resulting from a superposition of the single-crystal spectra at all orientations of the molecule with respect to the external magnetic field.

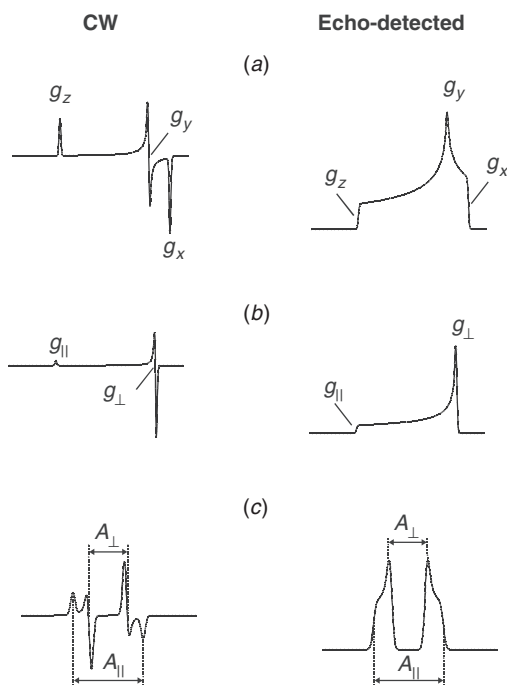


**Fig. 4.** Powder line shapes in continuous wave (CW) ESR (derivative absorption spectra) and echo-detected ESR (absorption spectra). (a) Rhombic g-tensor. (b) Axial g-tensor. (c) Axial hyperfine coupling tensor with dominating isotropic contribution.

established by theoretical considerations or by quantum chemical computations of the interaction tensors.

### 2.3. Isotropic Hyperfine Analysis

Anisotropic line broadening in solids often leads to a situation in which only one dominant hyperfine interaction is resolved, the one for the atom at which the spin is localized. In fluid media, however, anisotropic contributions average, lines are narrower, and a multitude of hyperfine interactions may be resolved. This situation is frequently observed for proton couplings in  $\pi$  radicals, where the electron spin is distributed throughout a network of conjugated bonds. Examples can be found in Ref. 23.

In isotropic ESR spectra, a single nucleus with spin  $I_k$  causes a splitting into  $2I_k + 1$  lines corresponding to the magnetic quantum numbers  $m_I = -I_k, -I_k + 1, \dots, I_k$ . For a group of  $n_k$  equivalent nuclei (same isotropic hyperfine coupling), the number of lines is  $2n_k I_k + 1$ . For groups of nonequivalent spins, the number of lines (multiplicities) increases, and the total number of lines in the ESR spectrum is given in Eq. 9.

$$N_{\text{ESR}} = \prod (2n_k I_k + 1) \quad (9)$$

An example is shown in Fig. 5, where the spectrum for an electron spin coupled to four protons ( $I = \frac{1}{2}$ ) exhibits a regular pattern of 16 lines. In complicated spectra consisting of multiple interacting nuclei, some of the smaller hyperfine couplings cannot be resolved. In such cases, ENDOR spectra are often easier to interpret, because each proton contributes only two lines; this technique is described in Chapter 2.

### 2.4. Environmental Effects on $g$ - and Hyperfine Interaction

Self-assembly of polymer chains is due to noncovalent interactions: hydrogen bonding,  $\pi$  stacking, and electrostatic and van der Waals interactions. The high sensitivity of the NMR chemical shift of protons to  $\pi$  stacking (through ring currents) and hydrogen bonding provides one way for their characterization.<sup>25</sup> Since the magnetic

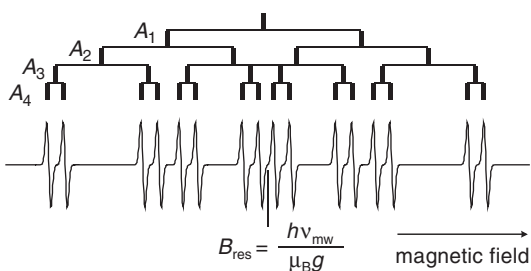


**Fig. 5.** Isotropic ESR spectrum for a system consisting of four nuclear spins  $I_k = \frac{1}{2}$  coupled to a single electron spin  $S = \frac{1}{2}$ .

parameters of paramagnetic probes are also sensitive to such interactions, ESR spectroscopy can confirm and complement the information obtained by NMR.

The hyperfine interaction is influenced by any environmental effect that can perturb the spin density distribution. For example, in nitroxide radicals the unpaired electron is distributed between the nitrogen ( $\approx 40\%$ ) and oxygen atom ( $\approx 60\%$ ) in the polar N–O bond (Fig. 6). This distribution can change in the vicinity of a polar molecule (polar solvent or ion). Generally, a more polar solvent (higher dielectric constant) leads to a higher spin density  $\rho_N$  on the nitrogen atom and thus to a larger observed hyperfine coupling.<sup>26</sup> The spin density distribution is also influenced by hydrogen bonding to the oxygen atom, which also increases the hyperfine coupling.

The same interactions affect the deviation of  $g_x$  from the free electron value  $g_e$ , but in the opposite direction, since the extent of spin–orbit coupling is proportional to the spin density  $\rho_O$  on the oxygen atom. However, the effect on  $g_x$  also depends on the lone-pair energy, whose lowering causes stronger spin–orbit coupling. The lone-pair energy in turn is more affected by hydrogen bonding than by the local polarity, so that compared to  $A_z$ ,  $g_x$  is more sensitive to hydrogen bonding than to polarity. Correlation of  $g_x$  to  $A_z$  thus enable the separation of polarity and hydrogen-bonding effects.<sup>26</sup> In principle, the same effects scaled by a factor of one-third can be seen in the isotropic values  $A_{\text{iso}}$  and  $g_{\text{iso}}$ , as the other principal values of the tensors are much less affected. As a rule, measurements of  $A_z$  and of  $g_x$  in solid samples at high field (W band) are much more precise than measurements of  $A_{\text{iso}}$  and  $g_{\text{iso}}$  at X-band frequencies.

## 2.5. Accessibility to Paramagnetic Quenchers

Spin exchange due to collision of paramagnetic species (see Section 2.1) can be used to check whether a spin-labeled site in a macromolecule is accessible by the solvent. To this end, a paramagnetic quencher is added to the solvent, and the effect on the spectrum or relaxation time of the spin label is measured. The quencher is a fast relaxing paramagnetic species, usually a molecule or transition ion complex with spin  $S > \frac{1}{2}$ . The situation is illustrated in Fig. 7 for oxygen as the quencher ( $S = 1$ , triplet ground state), which is soluble in nonpolar solvents and only moderately soluble in water. We can assume, without loss of generality, that at a certain time oxygen is in the  $T_{-1}$  triplet

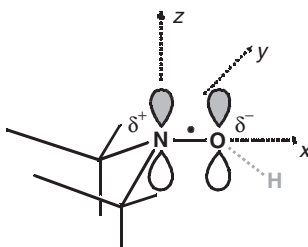


**Fig. 6.** Effects of the local polarity and hydrogen bonding on the nitroxide radical. The distribution of the unpaired electron between the two  $2p_z$  orbitals on nitrogen and oxygen is affected.

substate and the nitroxide label is in the  $\alpha$  state (spin up), which is the excited spin state for an electron (Fig. 7a). The two molecules diffuse and collide at a later time (Fig. 7b). Due to overlap of the wave functions, the three unpaired electrons become indistinguishable. Hence, when the two molecules separate again, there is a two-third's probability that the nitroxide is now with an unpaired electron in the  $\beta$  spin (spin down) and the oxygen molecule is in the  $T_0$  state (Fig. 7c). Effectively, the collision with the quencher has thus relaxed the nitroxide from its spin excited state to the spin ground state. This corresponds to longitudinal relaxation. If longitudinal relaxation of the quencher is sufficiently fast and collisions are sufficiently frequent, the longitudinal relaxation time  $T_1$  of the nitroxide is thus shortened. Indeed, the transverse relaxation time  $T_2$  is also shortened, although this cannot be understood in such a simple picture. Collisions with a paramagnetic quencher thus lead to line broadening and faster longitudinal relaxation.

The shortening of  $T_1$  is not directly visible in the ESR spectrum, but can be detected by saturation measurements with better sensitivity and higher precision than the shortening of  $T_2$ . In such CW ESR saturation measurements, the spectra are recorded as a function of mw power both in the presence and in the absence of the quencher. For nitroxides, a fit of the power dependence of the amplitude of the central line by a theoretical expression yields the parameter  $P_{1/2}$ , which is the power where the amplitude is reduced to one-half its value in the absence of saturation.<sup>27</sup> The difference of  $\Delta P_{1/2}$  values in the presence and absence of quencher is a measure for the accessibility of the spin label by the quencher. Normalization to the width of the central line and to the half

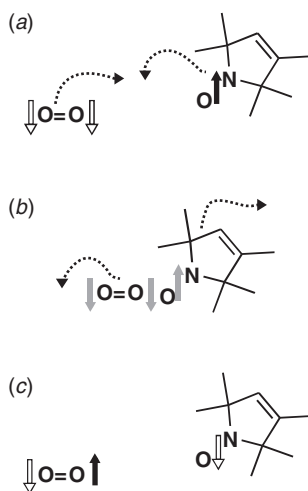


**Fig. 7.** Electron spin relaxation due to collision with a paramagnetic quencher. (a) An oxygen molecule in its  $T^{-1}$  state and a nitroxide with electron spin up are diffusing toward each other. (b) The two molecules collide and the three electrons are no longer distinguishable. (c) The two molecules have diffused apart after exchanging one electron. The oxygen molecule is now in its  $T^0$  state, while the nitroxide has spin down.

saturation power of a standard sample, such as diphenyl picrylhydrazyl (DPPH), yields a dimensionless accessibility parameter. Accessibility to nonpolar solvents can be tested by saturating the solution with nitrogen (no quencher) and air (20% oxygen), while accessibility to polar solvents, such as water, can be tested with chromium(III)oxalate.

## 2.6. Line Shape Analysis for Tumbling Nitroxide Radicals

The mobility of a spin probe depends on the local viscosity (microviscosity) and on its connectivity to a larger, more immobile object. For spin labels, the mobility depends on the flexibility of the tether connecting it to the backbone, and on tumbling of the macromolecule as a whole. The mobility can be quantified by the rotational correlation time  $\tau_r$ , which corresponds to the typical time during which a molecule maintains its spatial orientation. If the inverse of  $\tau_r$  is of the same order of magnitude as the anisotropy of an interaction, this anisotropy is partially averaged and the ESR spectrum depends strongly on  $\tau_r$  and on specific dynamics, such as the preference for a particular rotational axis or restrictions on the motion. For nitroxides at X-band, the ESR spectrum is dominated by the hyperfine anisotropy of  $\approx 150$  MHz. The largest effects are thus observed on time scales of a few nanoseconds, as illustrated in Fig. 8.

For rotational correlation times  $< 10$  ps, the nitroxide spectrum consists of three lines with equal widths and amplitudes (fast limit), and no information on  $\tau_r$  can be inferred from such spectra. For  $\tau_r$  in the range 10 ps–1 ns, the transverse relaxation and thus the line width are dominated by effects of rotational motion.<sup>28</sup> The spectrum still consists of three derivative Lorentzian lines, but they now have different amplitudes and widths. In this regime, the rotational correlation time can be inferred from the ratio of the line amplitudes.<sup>17</sup> In the range 1–10 ns, spectra are best analyzed by simulations. At even longer rotational correlation times, the anisotropy is only moderately reduced by motion and the spectrum is basically a powder spectrum with slightly reduced outer extrema separation  $2A'_{zz}$  (see spectrum at  $\tau_r = 32$  ns in Fig. 8). If the outer-extrema separation  $2A_{zz}$  in the rigid limit and the isotropic hyperfine coupling are known, for example, from measurements at very low and very high temperature,  $\tau_r > 3$  ns can be estimated with good precision from the relative anisotropy,  $A_{rel}$ :

$$A_{rel} = (2A'_{zz} - 2A_{iso}) / (2A_{zz} + 2A_{iso}) \quad (10)$$

A test for linearity in an Arrhenius plot of  $-\log(\tau_r)$  versus the inverse temperature reveals whether the dynamical process is an activated one.

For comparing dynamics in a series of materials, it is commonplace to plot the dependence of  $2A'_{zz}$  versus  $T$  rather than computing  $\tau_r$ . Such plots have a roughly sigmoidal shape (Fig. 9), with a maximum negative derivative close to  $2A'_{zz} = 50$  G that corresponds to a rotational correlation time of  $\approx 4$  ns. The corresponding temperature  $T_{50G}$  (or  $T_{5mT}$ ) is sometimes called ESR glass transition temperature (for a more detailed discussion, see Chapter 7).

Nitroxide radicals with  $\tau_r < 4$  ns thus give a liquid-type spectrum and are considered mobile (or fast), while nitroxide radicals with  $\tau_r > 4$  ns give a solid-type spectrum and are considered immobile (or slow). Polymers often exhibit distributions

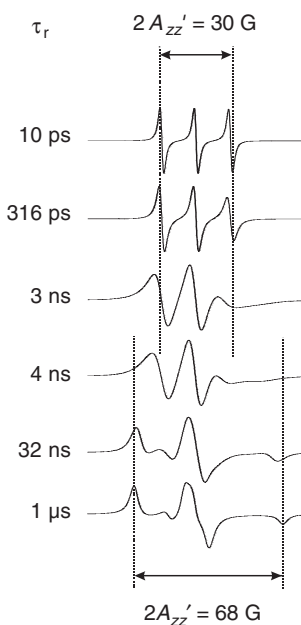


**Fig. 8.** Simulated nitroxide spectra at different rotational correlation times  $\tau_r$ . In the fast limit ( $\tau_r = 10$  ps) the outer-extrema splitting  $2A'_{zz}$  is approximately twice the isotropic hyperfine coupling; in the rigid limit ( $\tau_r = 10$   $\mu$ s) it is twice the hyperfine coupling along the molecular  $z$  axis (see Fig. 3).

of correlation times, so that the spectrum may contain both fast and slow components. Simulations show that the presence of two components in the spectra can be observed even for broad monomodal distributions of  $\tau_r$ , but in many cases it is due to genuinely bimodal distributions. This case is illustrated in Fig. 10 for a nitroxide radical in heterophasic poly(acrylonitrile–butadiene–styrene) (ABS); the fast and slow components in the ESR spectrum measured at 300 K are indicated, and represent radicals in butadiene-rich and acrylonitrile–styrene-rich domains, respectively; details will be described in Chapter 9.

### 3. MULTIFREQUENCY AND HIGH-FIELD ESR

Interpretation of solid-state ESR spectra may be difficult if several interactions in the Hamiltonian are of the same order of magnitude. Similarly, the spectrum of a tumbling nitroxide radical can often be reproduced by different motional models. In such cases, it may be impossible to analyze an ESR spectrum in an unambiguous way.

The problem can be overcome by measuring the spectrum not only at the standard frequency of  $\approx 9.4$  GHz (X band), where samples are most conveniently sized and spectrometers most available, but also at additional frequencies. For most organic

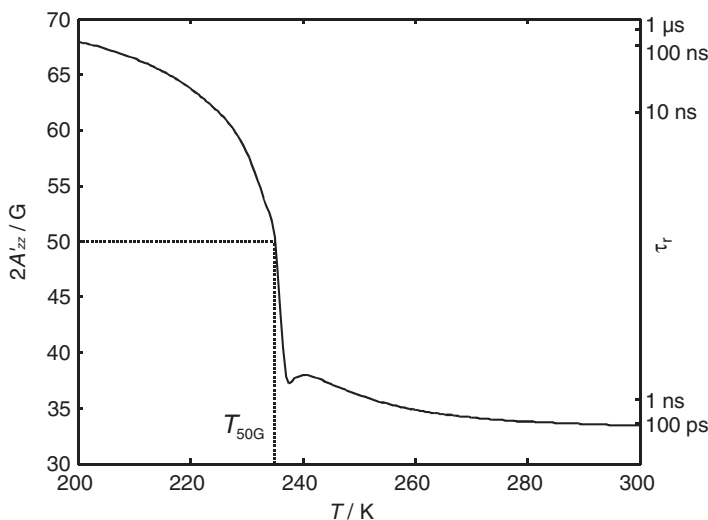


**Fig. 9.** Dependence of the outer-extrema splitting  $2A'_{zz}$  in nitroxide spectra on temperature (simulation for an activated process with activation energy of  $40 \text{ kJ mol}^{-1}$ ). At the temperature  $T_{50\text{G}}$ , where  $2A'_{zz} = 50 \text{ G}$ , the correlation time matches the inverse anisotropy of the spectrum.

radicals, the  $g$  resolution is at best mediocre at X band, and measurements at higher frequencies, such as Q band (35 GHz) and W band (95 GHz) are advantageous. Increasing the frequency is also useful for studies on nitroxide dynamics, since the  $g$ -tensor has lower symmetry than the hyperfine tensor. High-field (high-frequency) spectra therefore discriminate more strongly between different motional models. Even for transition metal complexes, frequencies  $> 10 \text{ GHz}$  may be advantageous if a small nonaxiality of the  $g$ -tensor has to be resolved. For spins  $S > \frac{1}{2}$  with relatively small ZFS, lines may become narrower at higher fields, since second-order broadening of the  $m_S = -\frac{1}{2} \leftrightarrow \frac{1}{2}$  transitions due to the ZFS decreases with increasing electron Zeeman interaction; this effect is prominent for Mn(II) complexes.

More advanced experiments, such as ENDOR, electron spin echo envelope modulation (ESEEM), or relaxation measurements by pulsed ESR rely on a selective excitation of spins close to the resonance field. Usually, the powder ESR spectrum is much broader than the excitation bandwidth of the pulses, which is in the range between 2 and 10 G. In cases where one anisotropic interaction dominates the spectrum, the experiments thus select contributions only from certain orientations of the molecule with respect to the external magnetic field. Such *orientation selection* is more efficient and easier to interpret at a field that is high enough for the  $g$  anisotropy to dominate. Finally, the size of mw resonators scales with wavelength and thus scales inversely with frequency. At higher frequency, spectra can thus be measured with much smaller sample volumes, yet the concentration does not need to be significantly increased.

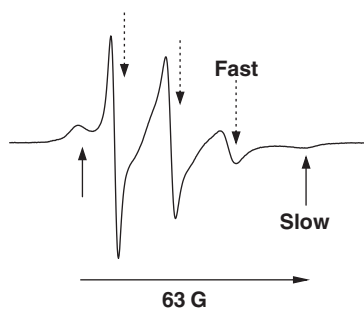


**Fig. 10.** X-band ESR spectrum at 300 K of a nitroxide radical derived from Tinuvin 770, a hindered amine stabilizer (HAS), in heterophasic ABS. Fast and slow components are indicated. The extreme separation of the slow component is 63 G.

In the case of transition metal complexes with large  $g$  anisotropy in disordered matrices, mw frequencies  $< 9.4$  GHz are sometimes preferable, because local heterogeneities (strain) of the matrix lead to a distribution of the principal values of the  $g$ - and  $A$ -tensors ( $g$ - and  $A$ -strain) and thus to field-dependent line broadening. Such a situation is illustrated in Fig. 11 for  $^{63}\text{Cu(II)}$  in Nafion perfluorinated ionomers swollen by acetonitrile:<sup>29</sup> the line width of the parallel components was measured at four mw frequencies in the range 1.2–9.4 GHz, and the narrowest line widths were detected for the two low-field lines of the parallel quartet at C band (4.7 GHz) and L band (1.2 GHz). In this way, clear superhyperfine splittings from  $^{14}\text{N}$  nuclei were resolved, in addition of course to the hyperfine splittings from  $^{63}\text{Cu(II)}$ .

Solving a problem by ESR spectroscopy may thus sometimes require access to spectrometers at several different frequencies, and in particular, to a high-frequency spectrometer. That said, it is good practice to first gather as much information as possible with the simplest technique, which is CW ESR at X band. After this step, it should be decided whether more information is required and how it can best be obtained.

#### 4. PULSED ESR METHODS

Continuous wave ESR is highly sensitive, applicable to most paramagnetic centers in a wide temperature range, and can be measured with relatively inexpensive spectrometers. However, quite often analysis of CW ESR spectra provides information only on one or two dominating interactions. Relaxation can be characterized to some extent by studying saturation of the spectrum at higher microwave power, but results are often only semiquantitative, as different contributions to spin relaxation cannot be separated. More information can be obtained by magnetic resonance experiments if pulsed instead of continuous irradiation is used, as demonstrated by the development of nuclear magnetic resonance (NMR) spectroscopy since the 1970s. The situation is somewhat less favorable in ESR spectroscopy, since in contrast to rf pulses in NMR,

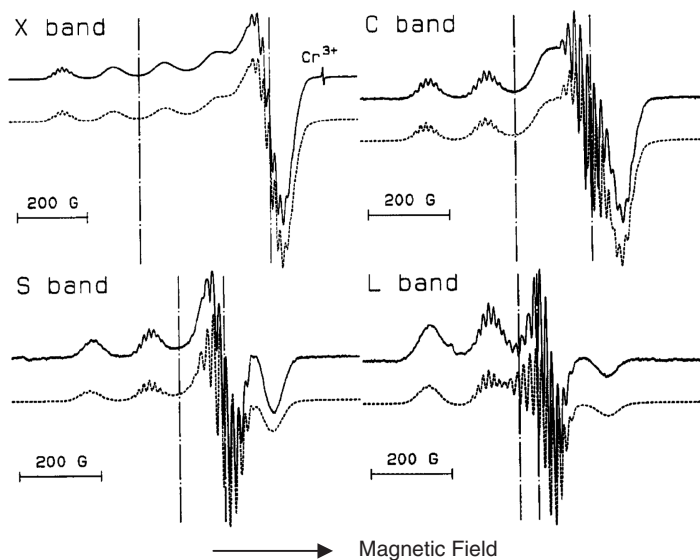


**Fig. 11.** Experimental (solid lines) and simulated (broken line) ESR spectra of  $^{63}\text{Cu}(\text{II})$  in Nafion perfluorinated membranes soaked by  $\text{CH}_3\text{CN}$  at the X band (9.36 GHz) and 110 K, and at the C band (4.7 GHz), S band (2.8 GHz), and L band (1.2 GHz) at 123. Vertical dashed lines indicate the position of  $g \parallel$ . Note the clearly visible superhyperfine splittings from nitrogen ligands at the lower than X-band frequencies.

mw pulses cannot usually excite the entire spectrum at once. For this reason, pulsed ESR is somewhat less sensitive than CW ESR for many samples and manipulation of the spin dynamics is somewhat less effective than in pulsed NMR. Nevertheless, pulsed ESR can be applied to most samples of interest and allows for a better separation of different interactions in the spin Hamiltonian, or the detection of different types of spin relaxation mechanisms, compared with CW ESR.<sup>8</sup>

Separation of interactions allows for precise measurements of the small interactions of the observed electron spin with remote spins in the presence of line broadening due to larger contributions. Such techniques are therefore most useful for solid materials or soft matter, where ESR spectra are usually poorly resolved. The most selective techniques for isolating one type of interaction from all the others are pulsed double resonance experiments, such as ENDOR and electron–electron double resonance (ELDOR), which are discussed in more detail in Chapter 2. If the hyperfine couplings are of the same order of magnitude as the nuclear Zeeman frequency, ESEEM techniques may provide higher sensitivity than ENDOR techniques. In particular, the two-dimensional hyperfine sublevel correlation (HYSCORE) experiment provides additional information that aids in the assignment of ESEEM spectra. These experiments are also discussed in Chapter 2.

The separation of different contributions to spin relaxation relies on echo experiments.<sup>30</sup> Spin echoes are also the basis for almost all other pulsed ESR experiments

in the solid-state and in soft matter, since the free induction signal induced by a single pulse usually decays within a time that is shorter than the receiver deadtime after that pulse. The simplest echo experiment is the two-pulse or Hahn echo experiment (Fig. 12), which consists of a first pulse with flip angle  $\pi/2$ , a delay  $\tau$ , and a second pulse with flip angle  $\pi$ . The first pulse converts the longitudinal magnetization of the spins that exists in thermal equilibrium to transverse magnetization. Initially, the contributions by all spins are in phase (coherent), but as different spins have different resonance offsets  $\Omega_S$ , they acquire a different phase  $\phi = \Omega_S\tau$  during time  $\tau$  and the signal thus vanishes. Additionally, magnetization within each packet of spins with equal resonance frequency decays by transverse relaxation with time constant  $T_2$ . The  $\pi$  pulse inverts the phase of each spin packet, which thus has the value  $-\phi$  immediately after that pulse. Within another delay  $\tau$ , each spin packet again acquires a phase  $\phi$ . This exactly cancels the phase differences, so that at time  $2\tau$  all spin packets are again coherent. This coherence corresponds to observable transverse magnetization, which is called a spin-echo signal. After time  $2\tau$ , the signal is a replica of the unobservable free induction decay (FID) signal after the first pulse, except for an attenuation of the total amplitude by a factor  $\exp(-2\tau/T_2)$ . By measuring the echo amplitude as a function of  $\tau$  (two-pulse echo decay),  $T_2$  can be determined.

If the formally forbidden electron-nuclear transitions are weakly allowed, the two-pulse echo decay is modulated by the corresponding nuclear frequencies. For a spin system of two weakly coupled electron spins, it is modulated with the coupling between the two spins. Measurement of the echo amplitude as a function of the external magnetic field  $B_0$  yields the absorption ESR line shape. This field-swept echo-detected ESR experiment is a useful alternative to CW ESR for systems with strong anisotropic line broadening. For example, in the situation in Fig. 4b the  $g_{\parallel}$  feature can be easily missed, in particular if it is broadened by  $g$  strain. The strong anisotropy is then revealed more clearly in the absorption line.

The longitudinal relaxation time  $T_1$  can be measured with the inversion recovery experiment that consists of a mw  $\pi$  pulse, a variable delay  $T$ , and a two-pulse echo

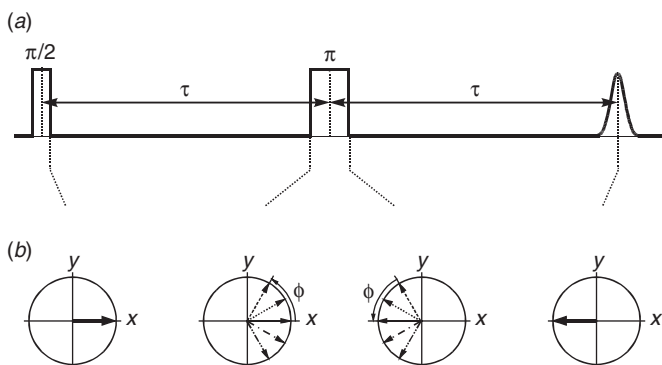


**Fig. 12.** Two-pulse echo experiment. (a) Pulse sequence. (b) Evolution of the magnetization vectors corresponding to spin packets with difference resonance offsets  $\Omega_S$ .

sequence with fixed delay  $\tau$ . The first  $\pi$  pulse inverts the longitudinal thermal equilibrium magnetization  $M_0$  to  $-M_0$ . During time  $T$  the longitudinal magnetization again relaxes toward  $M_0$  with time constant  $T_1$ . At the time of the  $\pi/2$  pulse of the echo subsequence, the longitudinal magnetization is thus given by  $[1-2 \exp(-T/T_1)]M_0$ . As only this longitudinal magnetization contributes to the echo experiment, the amplitude of the echo signal as a function of  $T$  is therefore proportional to  $1-2 \exp(-T/T_1)$ . The inversion recovery experiment may be affected by spectral diffusion: changes in the resonance frequency of the observed spins during delay time  $T$ . Such changes may result from reorientation of the molecules. If a paramagnetic center is not excited by the inversion pulse, changes its resonance frequency, and is then excited by the echo subsequence, it does not need to relax to contribute to the echo signal. To avoid this, the inversion pulse should have an excitation bandwidth that is larger than possible frequency changes by spectral diffusion. Alternatively, one can use a saturating pulse that is longer than the maximum delay time  $T_{\max}$ . Such a pulse excites all spins that are accessible by spectral diffusion within the time scale of the experiment. In this saturation recovery experiment, the echo amplitude is zero at  $T = 0$  and increases as  $1-\exp(-T/T_1)$ .

On the other hand, spectral diffusion may be the process of interest, as it is directly related to the dynamics of the paramagnetic centers. Spectral diffusion can be separated from longitudinal relaxation by first measuring  $T_1$  using the saturation recovery technique, and then measuring the decay of the stimulated echo with time  $T$  (Fig. 13), which is much more sensitive to spectral diffusion. As the two-pulse echo, the stimulated echo experiment starts with a  $\pi/2$  pulse that generates transverse magnetization and a subsequent delay  $\tau$  during which the magnetization acquires phase  $\phi = \Omega_S \tau$ . However, at this

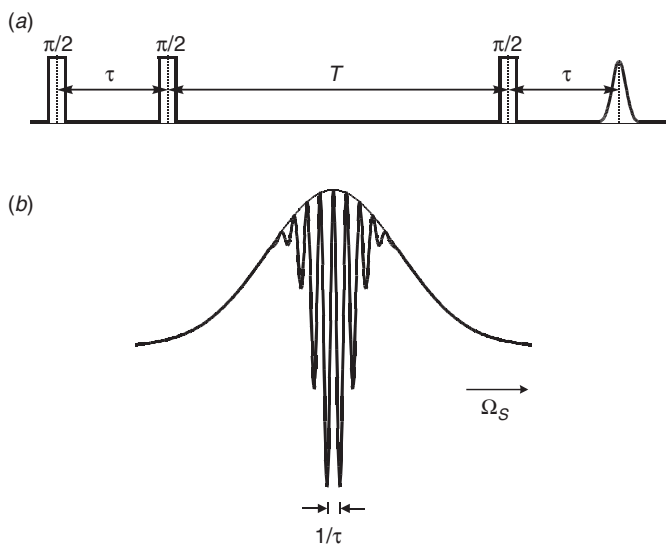


**Fig. 13.** Stimulated echo experiment. (a) Pulse sequence. (b) Polarization grating created by the first two  $\pi/2$  pulses with interpulse delay  $\tau$  in a Gaussian ESR line (simulation).

point a  $\pi/2$  pulse is applied instead of the  $\pi$  pulse of the two-pulse echo sequence. The  $\pi/2$  pulse converts transverse magnetization with zero phase ( $+x$ ) to negative longitudinal magnetization ( $-z$ ), it does not influence magnetization with phase  $+y$  ( $\phi = 90^\circ$ ) or  $-y$  ( $\phi = 270^\circ$ ), and it converts magnetization with phase  $-x$  ( $\phi = 180^\circ$ ) to positive longitudinal magnetization ( $+z$ ). As the magnetization before this pulse is equally distributed over the  $xy$  plane, only part of it is transferred to longitudinal magnetization. The remaining transverse magnetization decays much faster and does not contribute to the stimulated echo. If necessary, it can be eliminated by phase cycling of the pulses.<sup>8</sup> The longitudinal magnetization after the second  $\pi/2$  pulse is described by  $\cos(\Omega_S\tau)$ . By considering the limited excitation bandwidth of the pulses, this corresponds to a polarization grating as shown in Fig. 12*b*. During the following variable delay of duration  $T$ , the grating decays with time constant  $T_1$  due to longitudinal relaxation. In addition, changes in the resonance frequency of spin packets lead to exchange of polarization along the  $\Omega_S$  axis, that is, to a smearing of the grating. In the limit of much faster spectral diffusion compared to longitudinal relaxation, the grating is transformed to a broad unstructured hole in the ESR line that resembles the excitation profile of the  $\pi/2$  pulses.

The final  $\pi/2$  pulse transforms the longitudinal magnetization (polarization) to transverse magnetization. The subsequently detected signal can be considered as an FID of the polarization pattern. While the FID of a broad unstructured hole decays within the dead time after the pulse and cannot be observed, the FID of the polarization grating has the form of the Fourier transform of this grating. Since an oscillation with period  $1/\tau$  in angular frequency domain transforms to a delta peak at time  $\tau$  in time domain, this FID appears as an echo at time  $\tau$  after the last  $\pi/2$  pulse. As a function of delay  $T$ , the amplitude of this echo decays with  $\exp(-T/T_1)$ , but is additionally attenuated by spectral diffusion. The contribution by spectral diffusion can be easily recognized even if  $T_1$  is not known a priori, since the decay by spectral diffusion is faster for finer gratings, for longer interpulse delays  $\tau$ .

Additional pulsed ESR experiments have been used, which are beyond the scope of this introductory chapter. An overview of these experiments, as well as on the theoretical background of pulsed ESR, can be found in Ref. 8.

## ACKNOWLEDGMENTS

G. Jeschke gratefully acknowledges financial support by a Dozentenstipendium of Fonds der Chemischen Industrie. Research in the laboratory of S. Schlick is currently supported by grants from the Polymer Program of the National Science Foundation, the University Research Program of the Ford Motor Company, and the Fuel Cell Activity Center of General Motors.

## REFERENCES

1. Carrington, A.; McLachlan, A.D. *Introduction to Magnetic Resonance, with Applications to Chemistry and Chemical Physics*, Harper & Row: New York, 1967.
2. Alger, R.S. *Electron Paramagnetic Resonance: Techniques and Applications*, Wiley-Interscience: New York, 1968.

3. Abragam, A.; Bleaney, B. *Electron Paramagnetic Resonance of Transition Ions*, Clarendon: Oxford, UK, 1970.
4. Poole, C.P., Jr. *Electron Spin Resonance: A Comprehensive Treatise on Experimental Techniques*, 2nd ed., John Wiley & Sons, Inc.: New York, 1983.
5. Pilbrow, J.R. *Transition Ion Electron Paramagnetic Resonance*, Clarendon: Oxford, UK, 1990.
6. *Modern Pulsed and Continuous-Wave Electron Spin Resonance*, Kevan, L., Bowman, M.K., Eds.; John Wiley & Sons, Inc.: New York, 1990.
7. Weil, J.A.; Bolton, J.R.; Wertz, J.E. *Electron Paramagnetic Resonance: Elementary Theory and Practical Applications*; John Wiley & Sons, Inc.: New York, 1994.
8. Schweiger, A.; Jeschke, G. *Principles of Pulse Electron Paramagnetic Resonance*, Clarendon: Oxford, UK, 2001.
9. Wasserman, A.M. In *Specialist Periodical Reports — Electron Spin Resonance*; Gilbert, B.C., Davies M.J., Murphy D.M., Eds.; Royal Society of Chemistry: Cambridge, 1996; Vol. 15, pp. 115–152.
10. Goldfarb, D. In *Specialist Periodical Reports — Electron Spin Resonance*; Gilbert, B.C., Davies, M.J., Murphy, D.M., Eds.; Royal Society of Chemistry: Cambridge, 1996; Vol. 15, pp. 186–243.
11. Smirnov, A. In *Specialist Periodical Reports — Electron Spin Resonance*; Gilbert, B.C., Davies, M.J., Murphy, D.M., McLauchlan, K.A., Eds.; Royal Society of Chemistry: Cambridge, 2002; Vol.18, pp. 109–136.
12. Rånby, B.; Rabek, J.F. *ESR Spectroscopy in Polymer Research*, Springer-Verlag: Berlin, 1977.
13. *The Effects of Radiation on High-Technology Polymers*. Reichmanis, E., O'Donnell, J.H., Eds.; ACS: Washington, DC, 1989.
14. Hill, D.J.T.; Le, T.T.; O'Donnell, J.H.; Perera, M.C.S.; Pomery, P.J. In *Irradiation of Polymeric Materials: Processes, Mechanisms, and Application*; Reichmanis, E., Frank, C.W., O'Donnell, J.H., Eds.; ACS: Washington, DC, 1993.
15. Carswell, T.G.; Garrett, R.W.; Hill, D.J.T.; O'Donnell, J.H.; Pomery, P.J.; Winzor, C.L. In *Polymer Spectroscopy*; Fawcett, A.H., Ed.; Wiley: Chichester, UK, 1996; Chapt. 10, pp. 253–274.
16. *Macromolecule-Metal Complexes*; Ciradelli, F., Tsuchida, W., Wöhrle, D., Eds.; Springer: Berlin, 1996.
17. *Spin Labeling, Theory and Applications*; Berliner, L.J., Ed.; Academic Press: New York, 1976.
18. *Spin Labeling II, Theory and Applications*; Berliner, L.J., Ed.; Academic Press: New York, 1979.
19. *Biological Magnetic Resonance. Spin Labeling*; Berliner, L.J., Reuben, J., Eds.; Plenum: New York, 1989; Vol 8.
20. Motyakin, M.V.; Schlick, S. In *Instrumental Methods in Electron Magnetic Resonance, Biological Magnetic Resonance, Vol. 21*; Bender, C.J., Berliner, L.J., Eds.; Kluwer Academic/Plenum Publishing Corporation: New York, 2004; pp. 349–384.
21. *Molecular Motions in Polymers by E.S.R.*, Boyer, R.F., Keineth, S.E., Eds. Symposium Series Vol. 1; MMI Press: Harwood, Chur, 1980.
22. Cameron, G.G.; Davidson, I.G. In *Polymer Spectroscopy*; Fawcett, A.H., Ed.; John Wiley & Sons, Inc.: Chichester, UK, 1996; Chapt. 9, pp. 231–252.
23. Gerson, F.; Huber, W. *Electron Spin Resonance Spectroscopy of Organic Radicals*, Wiley-VCH: Weinheim, 2003.
24. Molin, Yu.N.; Salikhov, K.M.; Zamaraev, K.I. *Spin Exchange*, Springer: Berlin, 1980.

25. Spiess, H.W. *J. Polym. Sci. A* **2004**, *42*, 5031.
26. Owenius, R.; Engstrom, M.; Lindgren, M.; Huber, M. *J. Phys. Chem. A* **2001**, *105*, 10967.
27. Altenbach, C.; Greenhalgh, D.A.; Khorana, H.G., Hubbell, W.L. *Proc. Natl. Acad. Sci. USA* **1994**, *91*, 1667.
28. Nordio, P.L. In *Spin Labeling: Theory and Applications*; Berliner, L.J., Ed.; Academic Press: New York, 1976; Chapt. 2, pp. 5–52.
29. Bednarek, J.; Schlick, S. *J. Am. Chem. Soc.* **1991**, *113*, 3303.
30. Leporini, D.; Schädler, V.; Wiesner, U.; Spiess, H.W.; Jeschke, G. *J. Chem. Phys.* **2003**, *119*, 11829.